Opto-Electronic Advances

Supplementary information

November 2023, Vol. 6, No. 11

DOI: 10.29026/oea.2023.230133

Physics-data-driven intelligent optimization for large-aperture metalenses

Yingli Ha[1,2,3†], Yu Luo[1,2,3†], Mingbo Pu[1,2,3,4*], Fei Zhang[1,2,3], Qiong He[1,2], Jinjin Jin[1,2], Mingfeng Xu[1,2,3,4], Yinghui Guo[1,2,3,4], Xiaogang Li[5], Xiong Li[1,2,4], Xiaoliang Ma[1,2,4] and Xiangang Luo[1,2,3,4*]

[1]National Key Laboratory of Optical Field Manipulation Science and Technology, Chinese Academy of Sciences, Chengdu 610209, China; [2]State Key Laboratory of Optical Technologies on Nano-Fabrication and Micro-Engineering, Institute of Optics and Electronics, Chinese Academy of Sciences, Chengdu 610209, China; [3]Research Center on Vector Optical Fields, Institute of Optics and Electronics, Chinese Academy of Sciences, Chengdu 610209, China; [4]School of Optoelectronics, University of Chinese Academy of Sciences, Beijing 100049, China; [5]Tianfu Xinglong Lake Laboratory, Chengdu 610299, China.

[†]These authors contributed equally to this work.

*Correspondence: MB Pu, E-mail:pmb@ioe.ac.cn; XG Luo, E-mail: lxg@ioe.ac.cn

This file includes:

Section 1: Principle of adjoint-based shape optimization
Section 2: Inverse design network structure distribution.
Section 3: Training loss for smooth and rough regions.
Section 4: Overview of the FCN network architecture and training procedure.
Section 5: Simulated results of metalens with different diameters.
Section 6: Simulated results of metalens with different NA.
Section 7: The metalens fabrication process
Section 8: Optical setup for metalens measurements

Supplementary information for this paper is available at https://doi.org/10.29026/oea.2023.230133

Open Access This article is licensed under a Creative Commons Attribution 4.0 International License.
To view a copy of this license, visit http://creativecommons.org/licenses/by/4.0/.

© The Author(s) 2023. Published by Institute of Optics and Electronics, Chinese Academy of Sciences.

Section 1: Principle of adjoint-based shape optimization

The adjoint optimization method is a kind of gradient descent algorithm based on adjoint field physics. In each optimization process, the gradient information of the objective function in the whole parameter optimization space can be obtained only by calculating the forward field and the adjoint field once.

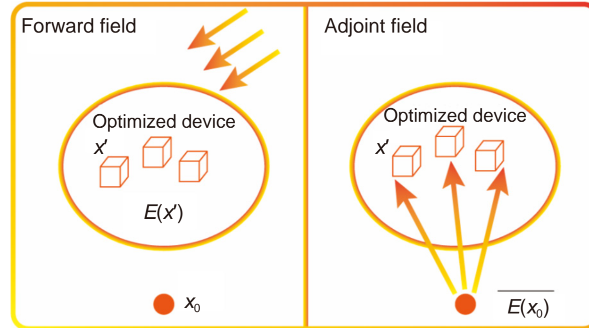

Fig. S1 | Schematic diagram of adjoint optimization.

Adjoint-based shape optimization is to optimize the geometric dimensions of binary patterns. As shown in Fig. S2, the initial structure boundary is a solid line, and the updated boundary is a dashed line. For a given deformation, the shadow area is ψ express. This figure can be regarded as a two-dimensional section of the deformation process of three-dimensional graphics. To region ψ, the integration needs to be carried out along the boundary of the initial pattern, and the deformation of the pattern needs to be along the normal direction of the boundary.

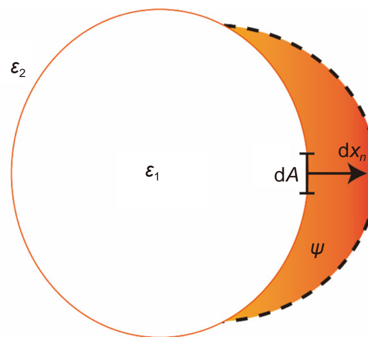

Fig. S2 | Schematic diagram of adjoint-based shape optimization.

The figure of merit (FOM) can be written as:

$$\delta FOM = 2\mathrm{Re}\int_{\psi} \boldsymbol{P}^{\mathrm{ind}}(x') \cdot \boldsymbol{E}^{A}(x')\mathrm{d}^3x' \ , \tag{S1}$$

where $\boldsymbol{P}^{\mathrm{ind}}$ is the induced dipole and $\boldsymbol{E}^{A}(x')$ is the adjoint electric field at the object location x'. According to the Fig. S2, dA is the derivative along the surface, and dx_{n} is the normal derivative, Eq. (S1) can be written as:

$$\delta FOM = 2\mathrm{Re}\int \mathrm{d}A \int \mathrm{d}x_n[\boldsymbol{P}^{\mathrm{ind}}(x') \cdot \boldsymbol{E}^{\mathrm{a}}(x')] \ , \tag{S2}$$

when the deformation tends to zero:

$$\int x_n \to \delta x_n(x') \ , \tag{S3}$$

where denotes the shape variable of the normal direction of each point on the boundary.

So:

$$\delta FOM = 2\mathrm{Re}\int \delta x_n(x')\boldsymbol{P}^{\mathrm{ind}}(x') \cdot \boldsymbol{E}^{\mathrm{a}}(x')\mathrm{d}S \ , \tag{S4}$$

According to the boundary conditions of Maxwell's equations, the tangential direction of $\boldsymbol{E}$ is continuous and the normal direction of $\boldsymbol{D}$ is continuous. Only in the continuous field, Eq. (S4) is meaningful. So the induced dipole can be

written as:

$$\boldsymbol{P}^{\mathrm{ind}}(x') = (\varepsilon_2 - \varepsilon_1)\boldsymbol{E}^{\mathrm{new}}(x') \ , \tag{S5}$$

where $\boldsymbol{E}^{\mathrm{new}}$ is the steady-state electric field of the deformed shape. Because even a small change in the boundary, the discontinuous component of $\boldsymbol{E}$ will change dramatically, so $\boldsymbol{E}^{\mathrm{new}} \cong \boldsymbol{E}^{\mathrm{old}}$ is not true, so:

$$\boldsymbol{E}^{\mathrm{new}} = \boldsymbol{E}_{||}^{\mathrm{old}} + \delta\boldsymbol{E}_{||} + \frac{\boldsymbol{D}_{\perp}^{\mathrm{old}} + \delta\boldsymbol{D}_{\perp}}{\varepsilon_2} \cong \boldsymbol{E}_{||}^{\mathrm{old}} + \frac{\boldsymbol{D}_{\perp}^{\mathrm{old}}}{\varepsilon_2} \ , \tag{S6}$$

Similarly, the adjoint electric field can be written as follows:

$$\boldsymbol{E}^{\mathrm{a}} = \boldsymbol{E}_{||}^{\mathrm{a}} + \frac{\boldsymbol{D}_{\perp}^{\mathrm{a}}}{\varepsilon_1} \ , \tag{S7}$$

So the change of FOM is written as:

$$\delta FOM = 2\mathrm{Re}\int \delta x_n(x')[(\varepsilon_2 - \varepsilon_1)\boldsymbol{E}_{||}^{f}(x') \cdot \boldsymbol{E}_{||}^{\mathrm{a}}(x') + (\frac{1}{\varepsilon_1} - \frac{1}{\varepsilon_2})\boldsymbol{D}_{\perp}^{f}(x') \cdot \boldsymbol{D}_{\perp}^{\mathrm{a}}(x')]\mathrm{d}S \ , \tag{S8}$$

From calculus:

$$\delta FOM = \sum_i \frac{\partial FOM}{\partial x_i}\delta x_i \ , \tag{S9}$$

For an optimization algorithm based on gradient:

$$\delta x_i = \frac{\partial FOM}{\partial x_i} \ , \tag{S10}$$

So, for all points x' prime on the boundary, the deformation in the normal direction can be expressed as:

$$\delta x_n(x') = 2\mathrm{Re}\left[(\varepsilon_2 - \varepsilon_1)\boldsymbol{E}_{||}^{f}(x') \cdot \boldsymbol{E}_{||}^{\mathrm{a}}(x') + \left(\frac{1}{\varepsilon_1} - \frac{1}{\varepsilon_2}\right)\boldsymbol{D}_{\perp}^{f}(x') \cdot \boldsymbol{D}_{\perp}^{\mathrm{a}}(x')\right] \ , \tag{S11}$$

$\boldsymbol{E}_{||}^{f}$ and $\boldsymbol{E}_{||}^{\mathrm{a}}$ denote the tangential components of the electric field obtained in the forward and adjoint simulations, respectively. $\boldsymbol{D}_{\perp}^{f}$ and $\boldsymbol{D}_{\perp}^{\mathrm{a}}$ denote the normal components of the potential shift-vector in the forward and adjoint simulations, respectively.

Section 2: Inverse design network structure distribution.

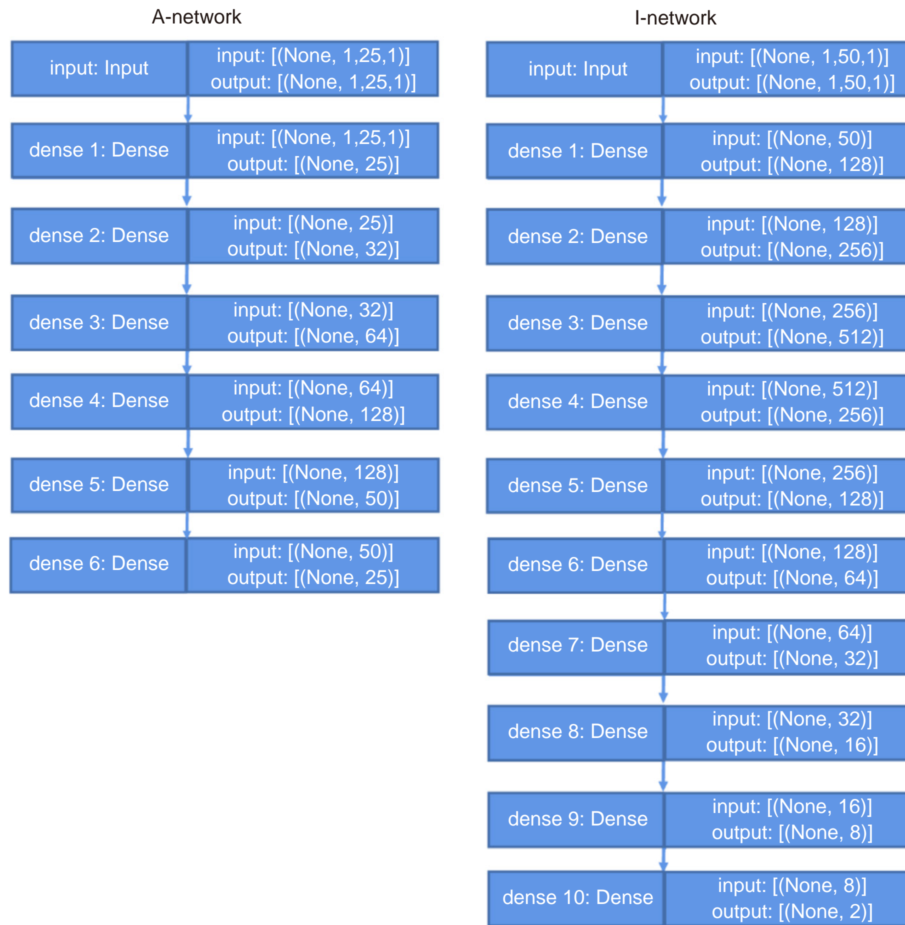

Fig. S3 | Network architectures. (**a**) A-network. (**b**) I-network.

Section 3: Training loss for smooth and rough regions.

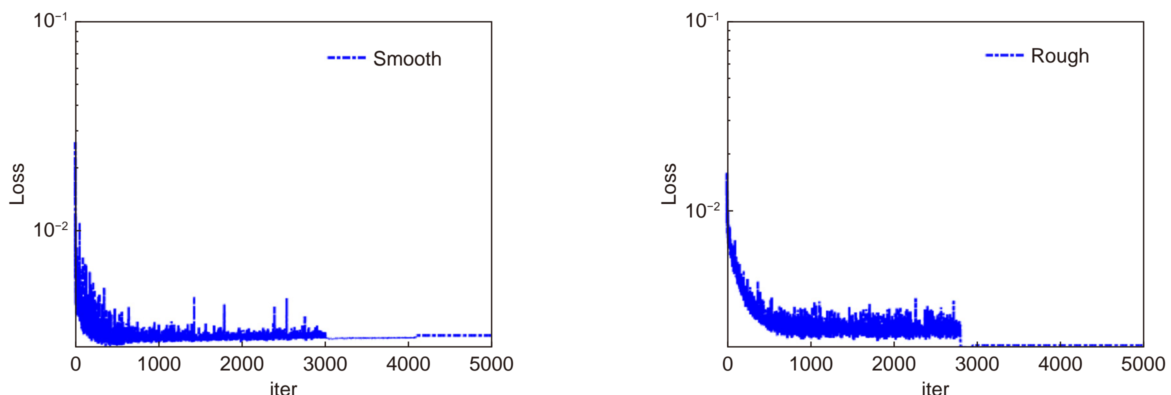

Fig. S4 | (**a**) Loss of different iterations for smooth region. (**b**) Loss of different iterations for rough region.

Section 4: Overview of the FCN network architecture and training procedure.

The fully connected neural (FCN) network is shown in Fig. S5(a), and one input data with a size of 5×5 is composed of the width/length of a super meta-atoms, while the output data with a size of 1×2 is composed of the width and length of the center meta-atom. As shown in Fig. S5(b), the network architectures of the FCN contain 5 layers, and the filter size of each layer is shown in Fig. S5(b). Figure S5(c) depicts the simulated dependence of loss value on the iteration number, and the loss eventually reaches the minimum (0.007) at the iteration of 5000.

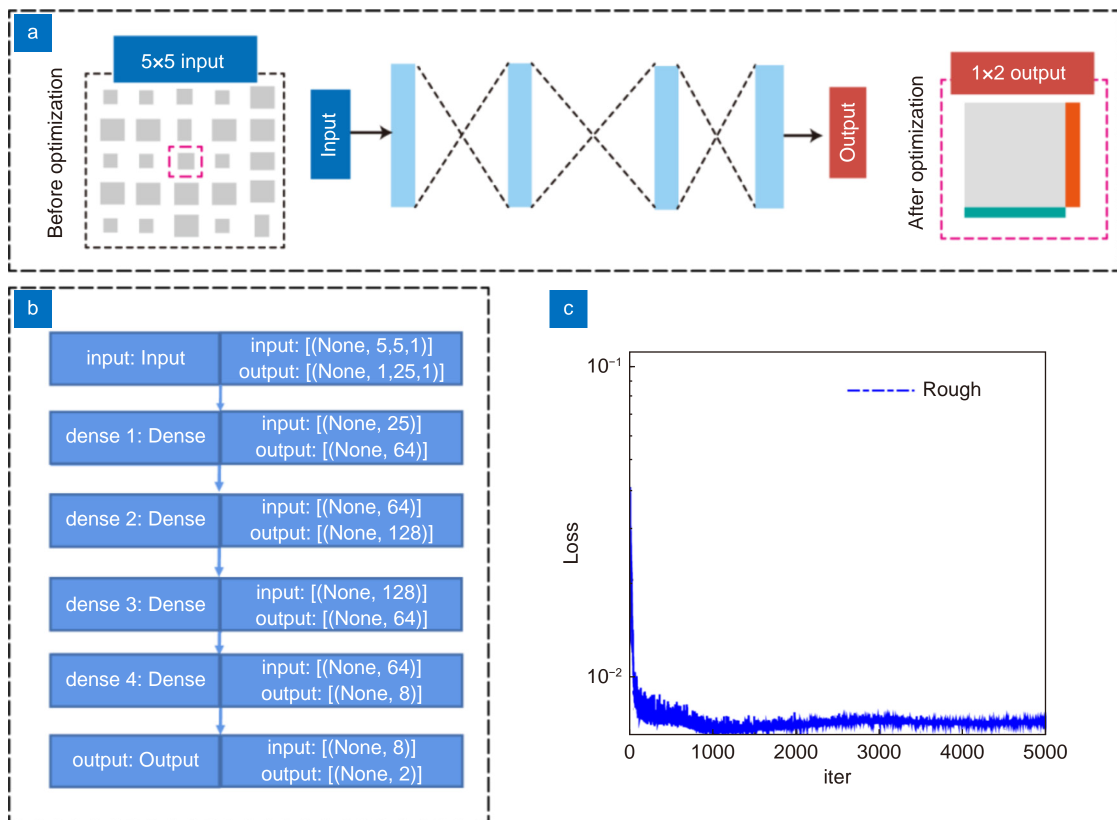

Fig. S5 | Overview of the FCN network architecture and training procedure. (a) Schematic of the FCN network. (b) The network architectures of the FCN. (c) The MAE loss for the smooth region.

Section 5: Simulated results of metalens with different diameters.

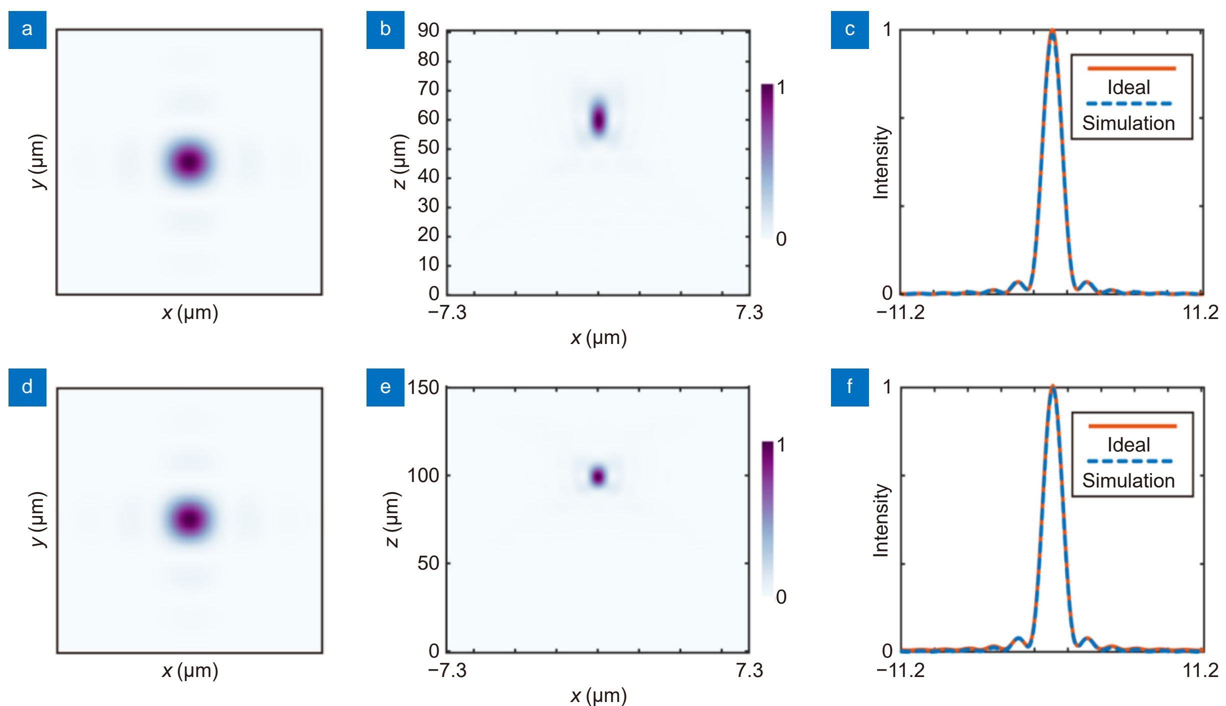

Fig. S6 | (**a**–**c**) Electric field distributions on *xy* and *xz* plane, and electric intensities of the focal spot for the metalens with the diameter of 60.5 μm; (**d**–**f**) Electric field distributions on *xy* and *xz* plane, and electric intensities of the focal spot for the metalens with the diameter of 100.5 μm.

Section 6: Simulated results of metalens with different NA.

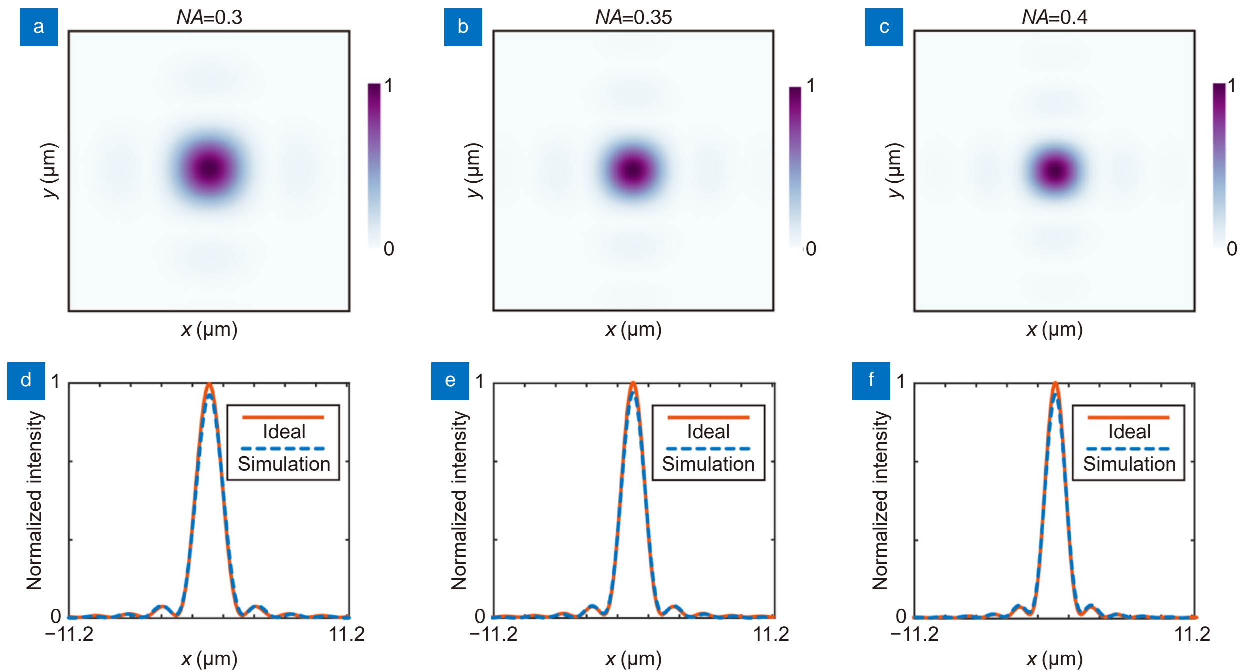

Fig. S7 | (a–c) Electric field distributions on *xy* plane for the metalens with the NA of 0.3, 0.35, and 0.4; (**d–f**) Normalized electric intensities of the focal spot for the metalens with the NA of 0.3, 0.35, and 0.4.

Section 7: The metalens fabrication process

The schematic of the metalens fabrication process is presented in Fig. S8. First, a 500 μm-thick Silicon on Sapphire (SOS) substrate was cleaned by the piranha solution followed by ultrasonic cleaning under acetone and isopropanol respectively. Next, a 100 nm-thick negative electron resist (ma-N2401, Micro resist technology) was spin-coated on the substrate and baked at 90 °C for 60 s. The electron beam patterning was performed by Elionix ELS-F125. The exposed sample was developed at room temperature for 10 s (ma-D 525, Micro resist technology). Then the inductively coupled plasma reactive ion etching (SENTECH SI 500) was employed to etch the silicon structures with SF_6 and C_4F_8 mixture and to remove the leaving electron resist.

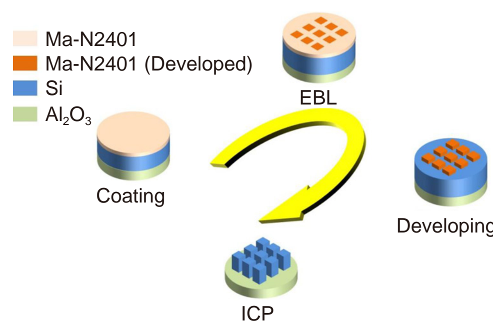

Fig. S8 | Schematic of the metalens fabrication process.

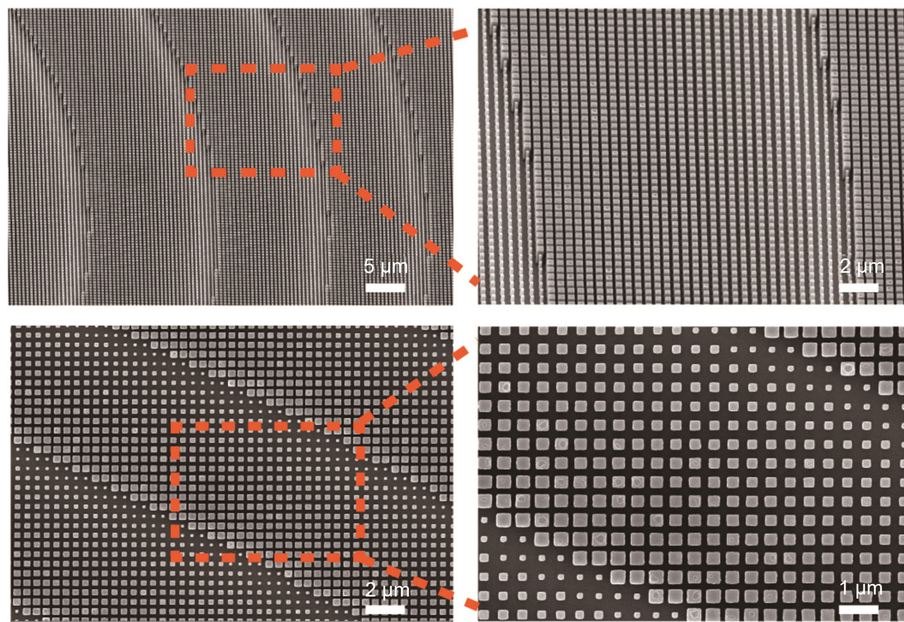

Fig. S9 | Scanning electron microscope image of the metalens with diameter of 1 mm.

Section 8: Optical setup for metalens measurements

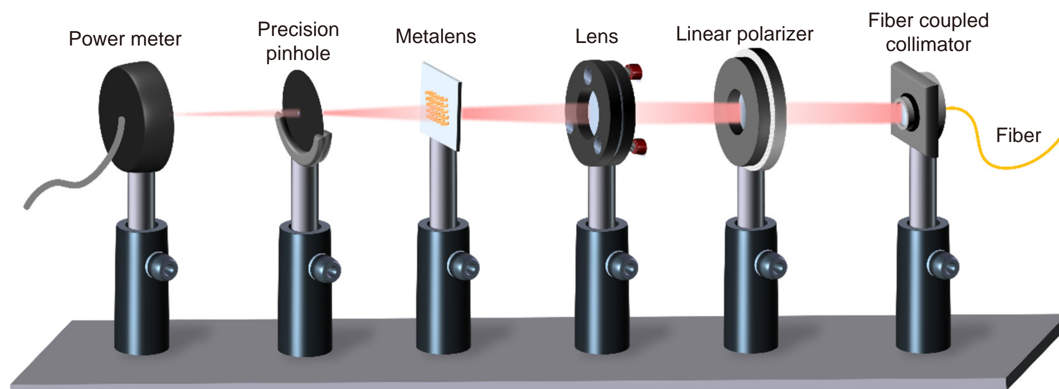

Fig. S10 | Schematic of the optical setup used to measure the focusing efficiency of the metalens. The fiber laser output 1550 nm line polarization beam is collimated by a fiber coupled collimator (Thorlabs, PAF2-A7C), liner polarizer is used to adjust the polarization state of the beam and adjust the laser intensity. A lens is used to adjust the size of laser beam. The adjusted laser beam with size same as the diameter of metalens. A precision pinhole (Edmund, Unmounted) is placed at metalens's focal length, the precision pinhole with 10 μm diameter to filter focus energy. A power meter is used to catch the energy incident on it.

We have measured relative focusing efficiency of the three sizes of metalens with different exposure doses. The relative focusing efficiency is defined as the ratio of the focusing power to the power of the focal plane, the focusing range is a circular area centered on the peak intensity, with a radius of treble full-width-half-maximums (FWHMs).

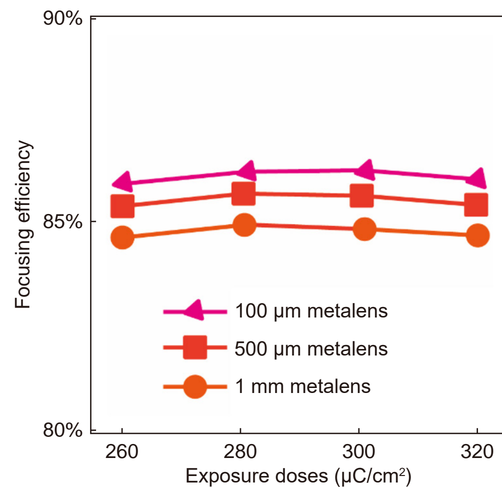

Fig. S11 | Measured focusing efficiency of three size metalens with different exposure doses.

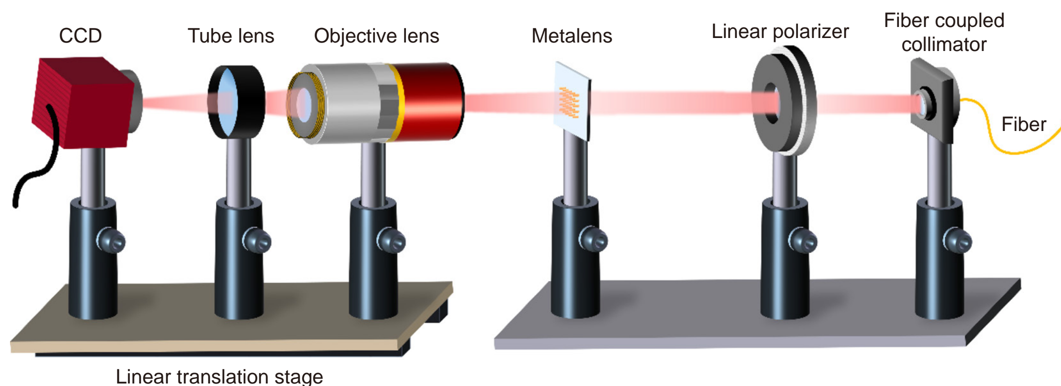

Fig. S12 | Schematic of the optical setup used to measure the focusing spot of the metalens. The fiber laser output 1550 nm line polarization beam is collimated by a fiber coupled collimator (Thorlabs, PAF2-A7C), liner polarizer is used to adjust the polarization state of the beam, then incident on the metalens. The microscopic imaging system is composed of a objective lens (Mitutoyo, 100× magnification), a tube lens (Edmund, MT-40) and a CCD camera (Allied Visio, G130), used to characterization the three-dimensional intensity distribution of the focal spot. The microscopic imaging system is installed on a linear translation stage.

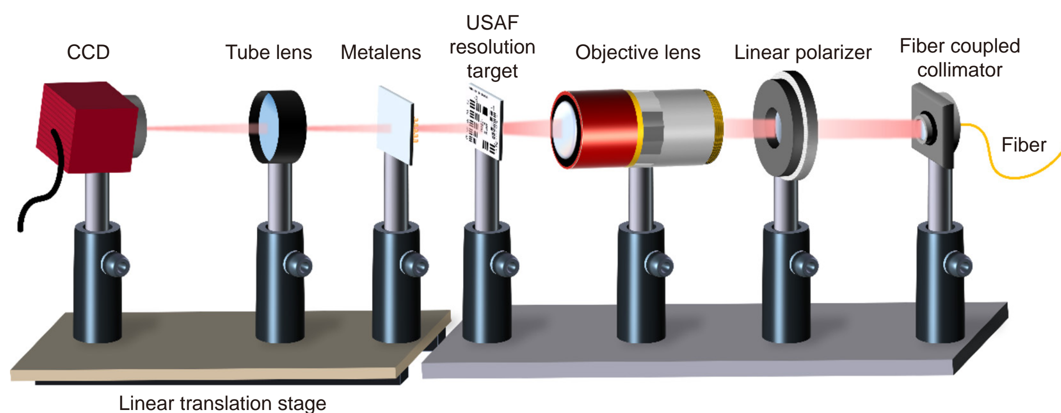

Fig. S13 | Schematic of the optical setup used to characterize the imaging performance of the metalens. The fiber laser output 1550 nm line polarization beam is collimated by a fiber coupled collimator (Thorlabs, PAF2-A7C), liner polarizer is used to adjust the polarization state of the beam, then incident on an objective lens (Mitutoyo objective, 10× magnification). The laser is focused by the objective lens and illuminated the United States Air Force resolution target (USAF resolution target). The metalens is placed parallel to the target, and the distance between them is the focal length of the metalens. The magnification imaging system is composed of metalens, a tube lens (Edmund, MT-40), and a CCD camera (Allied Visio, G032). The magnification imaging system is installed on a linear translation stage.